Received: 29 June 2023 | Revised: 22 August 2023 | Accepted: 2 September 2023

DOI: 10.1002/nbm.5055

RESEARCH ARTICLE

NMR IN BIOMEDICINE WILEY

Model resolution-based deconvolution for improved quantitative susceptibility mapping

Raji Susan Mathew | Naveen Paluru | Phaneendra K. Yalavarthy

Department of Computational and Data Sciences, Indian Institute of Science, Bangalore, Karnataka, India

Correspondence
Raji Susan Mathew, Department of Computational and Data Sciences, Indian Institute of Science, Bangalore, Karnataka, India.
Email: rajisusanm@iisc.ac.in

Funding information
CV Raman Postdoctoral Fellowship by Indian Institute of Science Bangalore.
Wipro-GE Collaborative Laboratory on Artificial Intelligence in Health Care and Medical Imaging.

Abstract

Quantitative susceptibility mapping (QSM) utilizes the relationship between the measured local field and the unknown susceptibility map to perform dipole deconvolution. The aim of this work is to introduce and systematically evaluate the model resolution-based deconvolution for improved estimation of the susceptibility map obtained using the thresholded k-space division (TKD). A two-step approach has been proposed, wherein the first step involves the TKD susceptibility map computation and the second step involves the correction of this susceptibility map using the model-resolution matrix. The TKD-estimated susceptibility map can be expressed as the weighted average of the true susceptibility map, where the weights are determined by the rows of the model-resolution matrix, and hence a deconvolution of the TKD susceptibility map using the model-resolution matrix yields a better approximation to the true susceptibility map. The model resolution-based deconvolution is realized using closed-form, iterative, and sparsity-regularized implementations. The proposed approach was compared with L2 regularization, TKD, rescaled TKD in superfast dipole inversion, the modulated closed-form method, and iterative dipole inversion, as well as sparsity-regularized dipole inversion. It was observed that the proposed approach showed a substantial reduction in the streaking artifacts across 94 test volumes considered in this study. The proposed approach also showed better error reduction and edge preservation compared with other approaches. The proposed model resolution-based deconvolution compensates for the truncation of zero coefficients in the dipole kernel at the magic angle and hence provides a closer approximation to the true susceptibility map compared with other direct methods.

KEYWORDS
dipole deconvolution, model-resolution matrix, reconstruction, susceptibility map, truncation parameter

Abbreviations used: COSMOS, calculation of susceptibility through multiple orientation sampling; HFEN, high-frequency error norm; NMSE, normalized mean squared error; PSNR, peak signal-to-noise ratio; QSM, quantitative susceptibility mapping; SSIM, structural similarity index measure; TKD, thresholded k-space division.

This work is supported by CV Raman Postdoctoral Fellowship by Indian Institute of Science Bangalore and Wipro-GE Collaborative Laboratory on Artificial Intelligence in Health care and Medical Imaging.

1 | INTRODUCTION

Quantitative susceptibility mapping (QSM) utilizes the relationship between the measured local field and the unknown susceptibility map to perform dipole deconvolution.[1–4] However, solving for the tissue susceptibility from the acquired phase data is intrinsically ill-posed because of the zero-valued coefficients around a double-shaped conical surface at the magic angle in the dipole kernel. One method to overcome this issue is the use of multiple orientation sampling data that leads to well-conditioned inversion, as in the case of calculation of susceptibility through multiple orientation sampling (COSMOS)[5] and susceptibility tensor imaging.[6] Although such multiorientation methods can yield near-optimal solutions, this requires a prohibitively high acquisition time and patient discomfort associated with collecting the data at different angular positions relative to the main magnetic field. Therefore, most of the practical QSM reconstruction methods rely on single-orientation acquisition with the utilization of prior information to stabilize the inversion. Broadly, the single-orientation methods can be grouped into three categories, namely, direct methods,[7,8] iterative methods,[9–11] and deep learning-based approaches.[12–14]

The most straightforward reconstruction approach is the thresholded k-space division (TKD) proposed by Shmueli et al.,[7] wherein the deconvolution is performed using a truncated dipole kernel whose entries are thresholded at a predetermined value (threshold) to avoid division by zero. Although the method is fast and simple, it can lead to undesirable streaking artifacts in the reconstructed susceptibility maps. This is due to the modification of the dipole kernel wherein the values less than the threshold are replaced with the threshold, and hence the division is performed with inflated values in the dipole kernel. To reduce these errors, a modified version of TKD was proposed by Schweser et al.,[15] wherein the susceptibility values obtained using TKD are rescaled using the maximum value of the point spread function (PSF) due to the dipole modification. Alternatively, a quadratic prior is introduced into the cost function to account for the zero-valued coefficients by Bilgic et al.[8] This often leads to over-smoothing and an unnatural appearance of the image. To overcome these limitations, a weighting in the k-space of the regularization term was introduced by Khabipova et al.,[16] such that the quadratic prior is applied only to the ill-conditioned k-space points. All methods discussed until now rely on the modification of the dipole kernel, which leads to artifacts in the reconstructed susceptibility map.

This work proposes a two-step formulation to reduce the artifacts introduced in the closed-form methods due to the modification of the dipole kernel based on a model-resolution matrix. Specifically, this work focuses on reducing the artifacts that appear in the susceptibility map generated using TKD due to the truncation of small coefficients in the dipole kernel. The TKD-estimated susceptibility map can be expressed as the weighted average of the true susceptibility map where the rows of the model-resolution matrix determine the weights, hence a deconvolution of the TKD susceptibility map using the model-resolution matrix yields a better approximation to the true susceptibility map. The model resolution-based deconvolution is realized using closed-form, iterative, and sparsity-regularized implementations. Experiments performed across 94 test volumes showed that the proposed approach consistently yields qualitatively and quantitatively more accurate QSM reconstructions compared with the other deconvolution methods considered in this study.

2 | METHODS

2.1 | Datasets

A brief description of the two datasets utilized in this work is provided here. Dataset-I consisted of a total of 60 scans collected from 12 healthy subjects, acquired at 3 T (nine datasets using Tim Trio, and three datasets using MAGNETOM Skyra, Siemens Healthineers, Forchheim, Germany) at five different head orientations.[13] A 3D single-echo gradient echo (GRE) scan was used to acquire the dataset with sequence parameters as follows: voxel size $= 1 \times 1 \times 1\,\text{mm}^3$, $TR = 33\,\text{ms}$, $TE = 25\,\text{ms}$, bandwidth $= 100\,\text{Hz/pixel}$, flip angle $= 15^0$. The field of views (FOVs) for the Tim Trio and Skyra scans were set to $256 \times 224 \times 176$ and $224 \times 224 \times 176\,\text{mm}^3$, respectively.[13] All imaging volumes in the dataset had a matrix size of $176 \times 176 \times 160$. Dataset-II consisted of eight healthy subjects, acquired at 7 T (Philips Achieva) with four head orientations each, with a total of 32 volumes.[17] Three slightly different 3D GRE sequences were used to acquire the dataset with voxel size $= 1 \times 1 \times 1\,\text{mm}^3$. The other sequence parameters were: $TR = 28\,\text{ms}$, $TE1/\delta TE = 5/5\,\text{ms}$, five echoes, FOV $= 224 \times 224 \times 126\,\text{mm}^3$ for the first four subjects, $TR = 45\,\text{ms}$, $TE1/\delta TE = 2/2\,\text{ms}$, nine echoes, FOV $= 224 \times 224 \times 110\,\text{mm}^3$ for the next three subjects and $TR = 45\,\text{ms}$, $TE1/\delta TE = 2/2\,\text{ms}$, 16 echoes, FOV $= 224 \times 224 \times 110\,\text{mm}^3$ for the last subject.[17] Among them, 16 volumes were of matrix sizes $224 \times 224 \times 126$, and the remaining 16 volumes were of matrix size $224 \times 224 \times 110$. Multiple phase preprocessing steps were performed for each dataset, including phase unwrapping,[18] brain masking with FSL BET,[19] and background phase removal using V-SHARP.[20,21] For the multiecho datasets, echo averaging was also performed for echoes with TEs between 10 and 30 ms. Dataset-I and Dataset-II were preprocessed and shared by Ref..[13] and Ref.,[17] respectively. The individual test data were referred to as subject 1 to 12 (Dataset-I) and subject 1 to 8 (Dataset-II), with the respective orientation number.

2.2 | Model resolution-based deconvolution

The measured local field $\delta_B(\mathbf{r}) \in \mathcal{P} \subseteq \mathbb{R}^p$ is related to the underlying unknown susceptibility map $\chi_{true}(\mathbf{r}) \in \mathcal{X} \subseteq \mathbb{R}^p$ as

$$\mathcal{F}^H D(\mathbf{k}) \mathcal{F} \chi_{true}(\mathbf{r}) = \delta_B(\mathbf{r}), \tag{1}$$

where $\mathcal{F}$ denotes the Fourier transform matrix, $D(\mathbf{k})$ denotes the diagonal matrix of size $p \times p$ with entries $\frac{1}{3} - \frac{k_z^2}{k^2}$, and $\mathcal{P}$ and $\mathcal{X}$ represent the spaces of local field measurements and susceptibility maps, respectively. Here $\mathbf{k}$ denotes the coordinate vector in the Fourier domain, $\mathbf{r}$ denotes the coordinate vector in the image domain, and $\mathbf{k}^2 = k_x^2 + k_y^2 + k_z^2$. Because $D(\mathbf{k})$ undersamples the frequency content of the susceptibility map as its entries are equal to zero on the conical surface, the inverse computation is highly ill-posed. To overcome this issue, TKD[7] performs the inversion using a truncated version of the dipole kernel, replacing those entries of D where the value is less than a constant number τ,

$$D_\tau^{-1}(\mathbf{k}) = \begin{cases} \left[\frac{1}{3} - \frac{k_z^2}{k^2}\right]^{-1}; if \left|\frac{1}{3} - \frac{k_z^2}{k^2}\right| > \tau \\ sgn\left[\frac{1}{3} - \frac{k_z^2}{k^2}\right] \tau^{-1}; otherwise \end{cases}. \tag{2}$$

Here *sgn* denotes the signum function. Then the susceptibility map $\widehat{\chi}^{TKD}(\mathbf{r})$ is estimated as

$$\widehat{\chi}^{TKD}(\mathbf{r}) = \mathcal{F}^H D_\tau^{-1}(\mathbf{k}) \mathcal{F} \delta_B(\mathbf{r}). \tag{3}$$

Substituting Equation (1) into Equation (3),

$$\widehat{\chi}^{TKD}(\mathbf{r}) = \mathcal{F}^H D_\tau^{-1}(\mathbf{k}) D(\mathbf{k}) \mathcal{F} \chi_{true}(\mathbf{r}). \tag{4}$$

Denoting

$$\mathcal{F}^H D_\tau^{-1}(\mathbf{k}) D(\mathbf{k}) \mathcal{F} = M, \tag{5}$$

which is called the model-resolution matrix, of size $p \times p$; Equation (4) can be represented as

$$\widehat{\chi}^{TKD}(\mathbf{r}) = M \chi_{true}(\mathbf{r}). \tag{6}$$

This indicates that the estimated susceptibility values are the weighted averages of the true susceptibility map, where the weights are determined by the rows of the model-resolution matrix.[22] Equation (6) can also be obtained in the following way. Denoting $\mathcal{F}^H D(\mathbf{k}) \mathcal{F}$ as $\mathcal{D}$ and $\chi_{true}(\mathbf{r})$ as X and $\delta_B(\mathbf{r})$ as $\mathcal{B}$, Equation (1) can be represented as

$$\mathcal{D}X = \mathcal{B}. \tag{7}$$

Multiplying Equation (7) using a preconditioner $\mathcal{T}$ yields,

$$\mathcal{T}\mathcal{D}X = \mathcal{T}\mathcal{B}. \tag{8}$$

In the proposed model-resolution approach, the preconditioner in Equation (8) is taken as the truncated inverse of $\mathcal{D}$ denoted as $\mathcal{D}_\tau^{-1} \left(= \mathcal{F}^H D_\tau^{-1}(\mathbf{k}) \mathcal{F}\right)$, which transforms the domain of the problem, that is,

$$\mathcal{D}_\tau^{-1} \mathcal{D} X = \mathcal{D}_\tau^{-1} \mathcal{B}, \tag{9}$$

where $\mathcal{D}_\tau^{-1}\mathcal{D}$ is the model-resolution matrix[23] denoted as M and $\mathcal{D}_\tau^{-1}\mathcal{B}$ is the estimated susceptibility map $\widehat{\chi}^{TKD}$. The model-resolution matrix is entirely determined by the operator matrix of the forward problem and is independent of the measured data (or noise therein). If $M = I$, where I is the identity matrix, the susceptibility values are exactly determined. However, as the model-resolution matrix is composed of the truncated version of the dipole kernel $D_\tau^{-1}(\mathbf{k})$, $M \neq I$. The diagonal entries that are not close to 1 indicate the deviation of estimated susceptibility maps from the true susceptibility maps. Dipole kernel $D_\tau(\mathbf{k})$ and the corresponding $D(\mathbf{k}) D_\tau^{-1}(\mathbf{k})$ for each truncation parameter are shown in Figure S1.

The aim of this work is to estimate $\chi_{true}(\mathbf{r})$ using M and $\widehat{\chi}^{TKD}(\mathbf{r})$. Because $\widehat{\chi}^{TKD}(\mathbf{r})$ can be expressed as the weighted average of the true susceptibility map, where the weights are determined by the model-resolution matrix as in Equation (6), the deconvolution of $\widehat{\chi}^{TKD}(\mathbf{r})$ using the model-resolution matrix yields a better approximation to the true susceptibility map. In other words, the second deconvolution is to reduce the errors introduced because of the truncation of the dipole kernel. The effect of dipole modification (truncating the dipole kernel) was investigated analytically by calculating the modulation transfer function (MTF) computed as $D_\tau^{-1}(\mathbf{k})D(\mathbf{k})$ in Ref.[15] which is equivalent to the model-resolution matrix, provided that Equation (1) is expressed in the Fourier domain. To estimate a closer approximation to the $\chi_{true}(\mathbf{r})$, Equation (6) is solved using (i) closed-form, (ii) iterative, and (iii) sparsity-regularized implementations.

2.2.1 | Closed-form solution

To estimate a closed-form solution for Equation (6), an approximate inverse M_τ^{-1} is first computed by taking $\left\{D_\tau^{-1}\right\}^{-1} \approx D$, and $D^{-1} \approx D_\tau^{-1}$, respectively. Thus, utilizing the dipole inverse in Equation (2), an estimate of $\chi_{true}(\mathbf{r})$ denoted as $\widehat{\chi}_{closed}(\mathbf{r})$ is computed as

$$\widehat{\chi}_{closed}(\mathbf{r}) = M_\tau^{-1}\widehat{\chi}^{TKD}(\mathbf{r}), \tag{10}$$

where M_τ^{-1} denotes the approximate inverse of M, computed as $M_\tau^{-1} = \mathcal{F}^{\mathrm{H}} D_\tau^{-1}(\mathbf{k})D(\mathbf{k})\mathcal{F}$. This step reduces the artifacts that are introduced in the TKD solution due to the truncation of small coefficients in the dipole kernel. The computation of the susceptibility map using TKD requires $\mathcal{O}(3p)$ operations and that of MR-TKD requires $\mathcal{O}(6p)$ operations, with reusing the matrix $\mathcal{F}^{\mathrm{H}} D_\tau^{-1}(\mathbf{k})$ from TKD. The truncation parameter τ to be used in the reconstruction of the proposed approach can be determined as that corresponding to the maximum contrast-to-noise ratio (CNR).[24,25] The computation of CNR was performed following the same procedure described in Ref.[25] Initially, the susceptibility difference $\Delta\chi = \chi_1 - \chi_2$ of the red nucleus and substantia nigra (χ_1) from the surrounding white matter (χ_2) was computed. Then the CNR was obtained as

$$\mathrm{CNR} = \frac{\mu\Delta\chi}{\sigma\Delta\chi}, \tag{11}$$

where $\mu\Delta\chi$ and $\sigma\Delta\chi$ denote the mean and standard deviation of $\Delta\chi$, respectively.

2.2.2 | Iterative solution

Although Equation (5) inversion can be achieved by a closed-form solution, M is ill-conditioned to be inverted, hence an iterative approach such as gradient descent is better suited, where the number of iterations acts as an implicit regularization.[18,26] To compute a closer approximation to the true susceptibility map in an iterative fashion, the optimization problem from Equation (6)

$$\underset{\chi_{true}(\mathbf{r})}{\operatorname{argmin}} \frac{1}{2}\left\| M\chi_{true}(\mathbf{r}) - \widehat{\chi}^{TKD}(\mathbf{r}) \right\|_2^2, \tag{12}$$

is solved using the gradient descent update,

$$\widehat{\chi}_i^{t+1}(\mathbf{r}) = \widehat{\chi}_i^{t}(\mathbf{r}) - \alpha M^H\left(M\widehat{\chi}_i^{t}(\mathbf{r}) - \widehat{\chi}^{TKD}(\mathbf{r})\right), \tag{13}$$

where α and t denote the step size and iteration number, respectively.

2.2.3 | Sparsity-regularized solution

To compute a sparsity-regularized solution for Equation (6), the optimization function is modified with the inclusion of the regularization function as

$$\underset{\chi_{true}(\mathbf{r})}{\operatorname{argmin}} \frac{1}{2}\left\| M\chi_{true}(\mathbf{r}) - \widehat{\chi}^{TKD}(\mathbf{r}) \right\|_2^2 + R(\chi_{true}(\mathbf{r})). \tag{14}$$

Then a proximal forward-backward splitting method is used where nonlinear diffusion (the nonlinear diffusion becomes equivalent to the total variation (TV) when the diffusivity function (g) used is $g(|\nabla\chi|)=\frac{1}{|\nabla\chi|+\epsilon}$,[27] where ∇ denotes the gradient operator and $\epsilon=10^{-6}$) forms the forward step and biasing (enforcing data consistency) forms the backward step. This is solved iteratively using,

$$\tilde{\chi}_s^{t+1}(\mathbf{r})=\hat{\chi}_s^{t}(\mathbf{r})-\alpha M^H\left(M\hat{\chi}_s^{t}(\mathbf{r})-\hat{\chi}^{TKD}(\mathbf{r})\right), \tag{15}$$

and

$$\hat{\chi}_s^{t+1}(\mathbf{r})=\tilde{\chi}_s^{t+1}(\mathbf{r})+\gamma div\left(g\left(\nabla\tilde{\chi}_s^{t+1}(\mathbf{r})\right)\nabla\tilde{\chi}_s^{t+1}(\mathbf{r})\right), \tag{16}$$

where *div* denotes the divergence operator, and γ is the regularization parameter.

2.3 | Figure of merit and comparison methods

The metrics considered in this work were structural similarity index measure (SSIM), peak signal-to-noise ratio (PSNR), normalized mean squared error (NMSE), and high-frequency error norm (HFEN), with all metrics computed with reference to COSMOS, as described in Langkammer et al.[28]

The proposed approach was compared with the L2 regularized method,[8] TKD,[7] the rescaled TKD in superfast dipole inversion (SDI)[15] referred to as the SDI, modulated closed-form (MCF)[16] method, iterative dipole inversion (Iterative DI), and that with TV prior (DI-TV). In L2-regularized reconstruction (L2)[8] Tikhonov formulation is utilized to obtain a closed-form solution computed as

$$\tilde{\chi}_{L2}(\mathbf{r})=\mathcal{F}^{\mathrm{H}}\left\{\frac{D(\mathbf{k})}{D(\mathbf{k})^2+\lambda^2\sum_{i=1}^{3}E_i^2}\mathcal{F}\delta_B(\mathbf{r})\right\}, \tag{17}$$

where λ is the regularization parameter, E_i is a diagonal matrix with entries given by $1-e^{-2\pi jk_i/N_i}$, and k_i and N_i are the k-space coordinate and the matrix size along i-direction, respectively. In SDI,[15] the value of the PSF at the origin, $PSF(\tau;\mathbf{0})$, is used to scale the TKD solution as

$$\tilde{\chi}_{SDI}(\mathbf{r})=[PSF(\tau;\mathbf{0})]^{-1}\hat{\chi}^{TKD}(\mathbf{r}), \tag{18}$$

where $PSF(\tau;\mathbf{r})=\mathcal{F}^{\mathrm{H}}D_{\tau}^{-1}(\mathbf{k})D(\mathbf{k})$. In MCF, a weighted form of Tikhonov regularization can be computed as

$$\tilde{\chi}_{MCF}(\mathbf{r})=\mathcal{F}^{\mathrm{H}}\left\{\frac{D(\mathbf{k})}{D(\mathbf{k})^2+\lambda^2\Lambda(\mathbf{k})\sum_{i=1}^{3}E_i^2}\mathcal{F}\delta_B(\mathbf{r})\right\}, \tag{19}$$

where $\Lambda(\mathbf{k})$ is a weighting matrix given by

$$\Lambda(\mathbf{k})=\begin{cases}\cos\frac{\frac{\pi}{2}D(\mathbf{k})}{\tau}; if\ |D(\mathbf{k})|<\tau\\ 0\qquad\quad ; otherwise.\end{cases} \tag{20}$$

Iterative DI solves the optimization problem,

$$\underset{\chi_{true}(\mathbf{r})}{\operatorname{argmin}}\frac{1}{2}\|A\chi_{true}(\mathbf{r})-\delta_B(\mathbf{r})\|_2^2, \tag{21}$$

using the gradient descent update,

$$\hat{\chi}_{DI}^{t+1}(\mathbf{r})=\hat{\chi}_{DI}^{t}(\mathbf{r})-\alpha A^H\left(A\hat{\chi}_{DI}^{t}(\mathbf{r})-\delta_B(\mathbf{r})\right), \tag{22}$$

where $A=\mathcal{F}^{\mathrm{H}}D(\mathbf{k})\mathcal{F}$. With regularization prior, the optimization problem takes the form,

$$\underset{\chi_{true}(\mathbf{r})}{\operatorname{argmin}} \frac{1}{2}\|A\chi_{true}(\mathbf{r}) - \delta_B(\mathbf{r})\|_2^2 + R(\chi_{true}(\mathbf{r})). \tag{23}$$

Then the above equation is solved iteratively using,

$$\tilde{\chi}_{DI-TV}^{t+1}(\mathbf{r}) = \hat{\chi}_{DI-TV}^{t}(\mathbf{r}) - \alpha A^H\left(A\hat{\chi}_{DI-TV}^{t}(\mathbf{r}) - \delta_B(\mathbf{r})\right), \tag{24}$$

and

$$\hat{\chi}_{DI-TV}^{t+1}(\mathbf{r}) = \tilde{\chi}_{DI-TV}^{t+1}(\mathbf{r}) + \gamma div\left(g\left(\nabla\tilde{\chi}_{DI-TV}^{t+1}(\mathbf{r})\right)\nabla\tilde{\chi}_{DI-TV}^{t+1}(\mathbf{r})\right). \tag{25}$$

The parameter values utilized in the reconstruction of each method were chosen to yield the minimum NMSE (averaged) across Dataset-I and Dataset-II and are summarized in Table S1 for reference. In all the iterative methods, the initial susceptibility vector is initialized as a zero vector. All implementations were performed using MATLAB on a Linux workstation with an Intel i9-10900 × 3.70 GHz processor and 128 GB of RAM.

3 | EXPERIMENTS

3.1 | Closed-form model resolution-based deconvolution

In this section, a brief description of the experiments performed for the selection of truncation parameters and comparison with other closed-form methods are provided. For the former case, the selection of the optimal truncation parameter using COSMOS, its generalizability (to other subjects, orientations, and acquisition protocols), and closeness to the parameter corresponding to maximum CNR, was examined by performing the following set of experiments. To compute the optimal truncation parameter and analyze its generalizability across different subjects under the same acquisition parameters, closed-form reconstructions (using Equation 10) were performed, with the values of τ varying from 0.10 to 0.50 in steps of 0.02 for subjects 1 to 6 of Dataset-I and Dataset-II. The head orientation (orientation 1) was kept the same for all subjects. Similarly, to compute the optimal truncation parameter and analyze its generalizability across different head orientations of the same subject, MR-TKD reconstructions were performed with τ values varying from 0.10 to 0.50 using Subject-1 of Dataset-I with head orientations 1 to 5 and Dataset-II with head orientations 1 to 4. To evaluate the closeness of the NMSE optimal parameter and that given by maximum CNR, the CNR values were computed with the values of τ varying from 0.10 to 0.50 with different subjects with the same orientation and different orientations of the same subjects for both Dataset-I and Dataset-II. To compare the performance of existing closed-form methods with the proposed closed-form method (using Equation 10), reconstructions were performed using L2, MCF, SDI, TKD, and the proposed closed-form method, using Dataset-II (Subject-3). It is to be noted that the rescaled TKD in SDI[15] is referred to as SDI here.

3.2 | Iterative and sparsity-regularized model resolution-based deconvolution

In this section, a brief description of the experiments performed for choosing the optimal scale factor, stopping criterion, and comparison with other methods, is provided. To choose the optimal scale factor, model resolution-based iterative deconvolution was performed with the scale factor values varying from 0.05 to 0.50 for subjects 1 and 2 of both datasets. To determine the stopping criterion, NMSE and relative gradient norms were computed at the prefixed scale factor for subjects 1 to 6 of Dataset-I and Dataset-II. For the chosen scale factor, the iterations were stopped when the relative change in gradient vectors is less than a tolerance, fixed empirically. In both cases, the reconstructions were performed for subjects 1 to 6 of Dataset-I. The performances of the proposed iterative and sparsity-regularized implementations were compared with iterative DI and DI-TV reconstructions.

4 | RESULTS

4.1 | Visual and figure of merit comparison

The representative reconstructed susceptibility maps and difference images using Dataset-II for different closed-form dipole deconvolution methods are shown in Figure 1. The susceptibility maps obtained using L2 were over-smoothed, whereas the ones for TKD, SDI, and MCF were

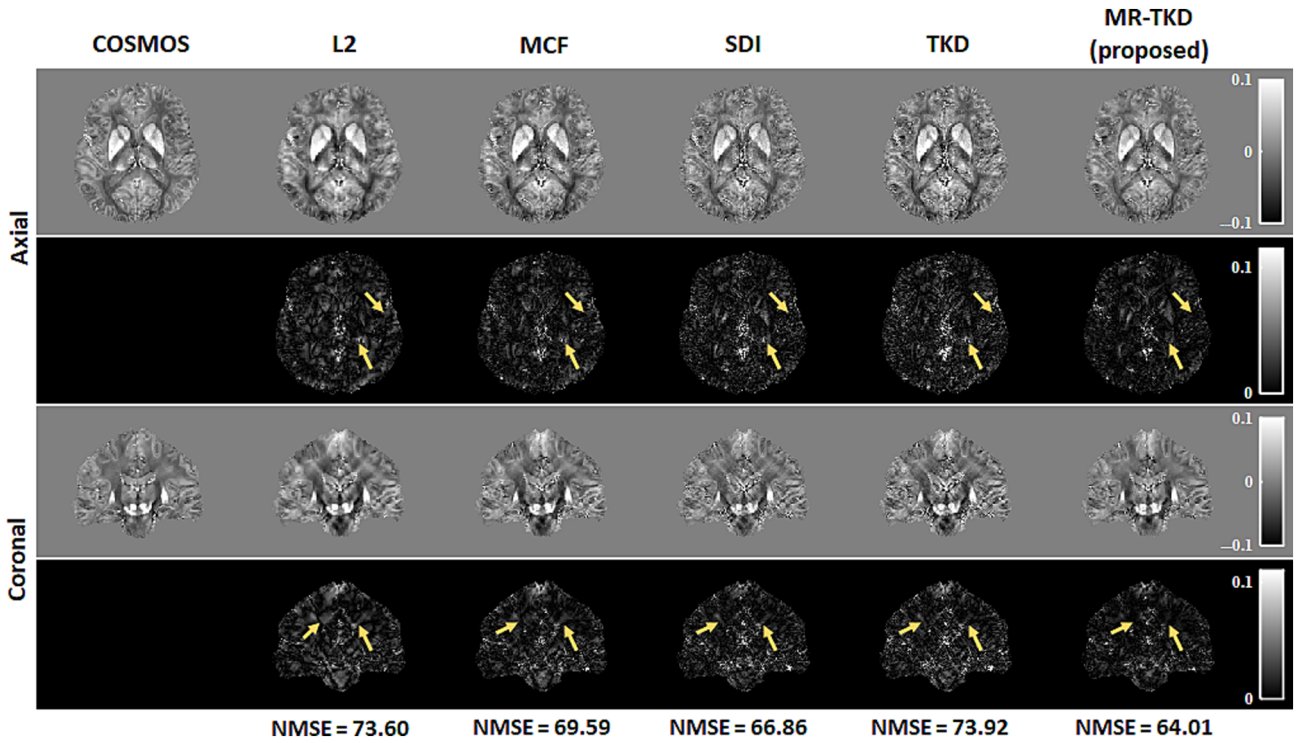

FIGURE 1 The first and third rows correspond to the axial and coronal views of the susceptibility maps reconstructed using different closed-form methods (listed at the top of the first row) for one representative subject in orientation-1 of Dataset-II. The corresponding difference images with respect to COSMOS (first column) are shown in the second and fourth rows, respectively. The NMSE values (with respect to COSMOS) for each volume are listed at the bottom for reference. COSMOS, calculation of susceptibility through multiple orientation sampling; MCF, modulated closed-form; MR-TKD, model resolution based truncated k-space division; NMSE, normalized mean squared error; SDI, superfast dipole inversion; TKD, thresholded k-space division.

sharper but with undesirable streaking artifacts. The images obtained using the MR-TKD yielded a better compromise between the mitigation of artifacts and image sharpness along with lower NMSE values (listed below the difference images). The representative reconstructed susceptibility maps and difference images using reconstruction challenge-1 (RC-1) data[28] and reconstruction challenge-2 (Sim1Snr1) data[29] of the dipole deconvolution methods are shown in Figures 2 and 3, respectively. The images obtained using the model resolution-based deconvolution yielded a better compromise between the mitigation of artifacts and image sharpness. It is to be noted that the model-resolution deconvolution proposed in this work used the TKD susceptibility map for the first deconvolution. The average figure of merit values for the different reconstruction methods are listed in Table 1. Compared with other methods, the proposed MR-TKD showed improvements in all metrics for both datasets.

4.2 | Local measurements

The local measurements of susceptibility values for five different regions of interest (ROIs) for different reconstruction methods and the respective COSMOS values are summarized in Table 2. The metrics values obtained using the proposed model resolution-based deconvolution were comparable with those of COSMOS for the different local regions considered.

4.3 | Selection and generalizability of truncation parameter for closed-form implementation

As reported for TKD,[7] the optimal parameter value for closed-form implementation (MR-TKD) lies in the range of 0.20 to 0.50. Plots of NMSE and CNR versus truncation parameters (τ) are shown in Figure S2. Plots of NMSE versus τ shown in Figure S2 (A1) and (A3) indicate that the optimal parameter (i.e., the parameter corresponding to the minimum NMSE) for all six subjects (with the same orientation) lies between 0.20 and 0.30, for Dataset-I and Dataset-II, respectively. The corresponding plots for CNR versus τ are shown in Figure S2 (A2) and (A4). It was observed that the truncation parameter corresponding to the maximum CNR, which provided a good trade-off between image contrast and noise amplification, lies close to the optimal parameter. Similarly, the NMSE versus τ plots for the same subject with different head orientations shown

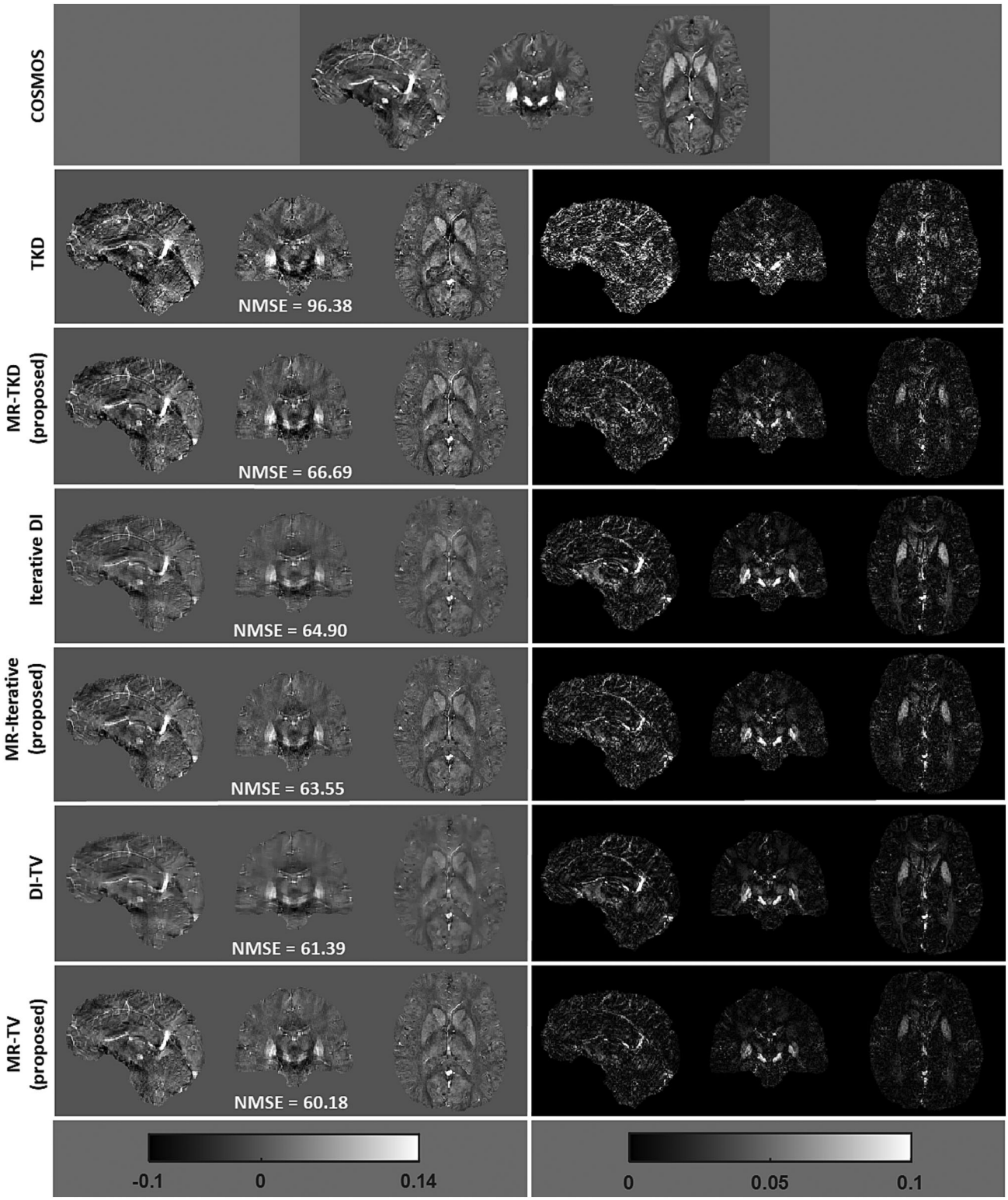

FIGURE 2 Reconstructed susceptibility maps (sagittal, coronal, and axial views) as the first column, and corresponding difference images with respect to COSMOS as the second column, obtained using the closed-form (rows 2 and 3), iterative (rows 4 and 5), and sparsity-enforced methods (rows 6 and 7) for reconstruction challenge-1 data. The COSMOS susceptibility maps are shown in the top row for reference. The NMSE values with respect to COSMOS are also shown in the insets. COSMOS, calculation of susceptibility through multiple orientation sampling; DI, dipole inversion; DI-TV, dipole inversion with total variation prior; MR, iterative; MR-TKD, model resolution based truncated k-space division; MR-TV, model resolution deconvolution with total variation prior; NMSE, normalized mean squared error; TKD, thresholded k-space division.

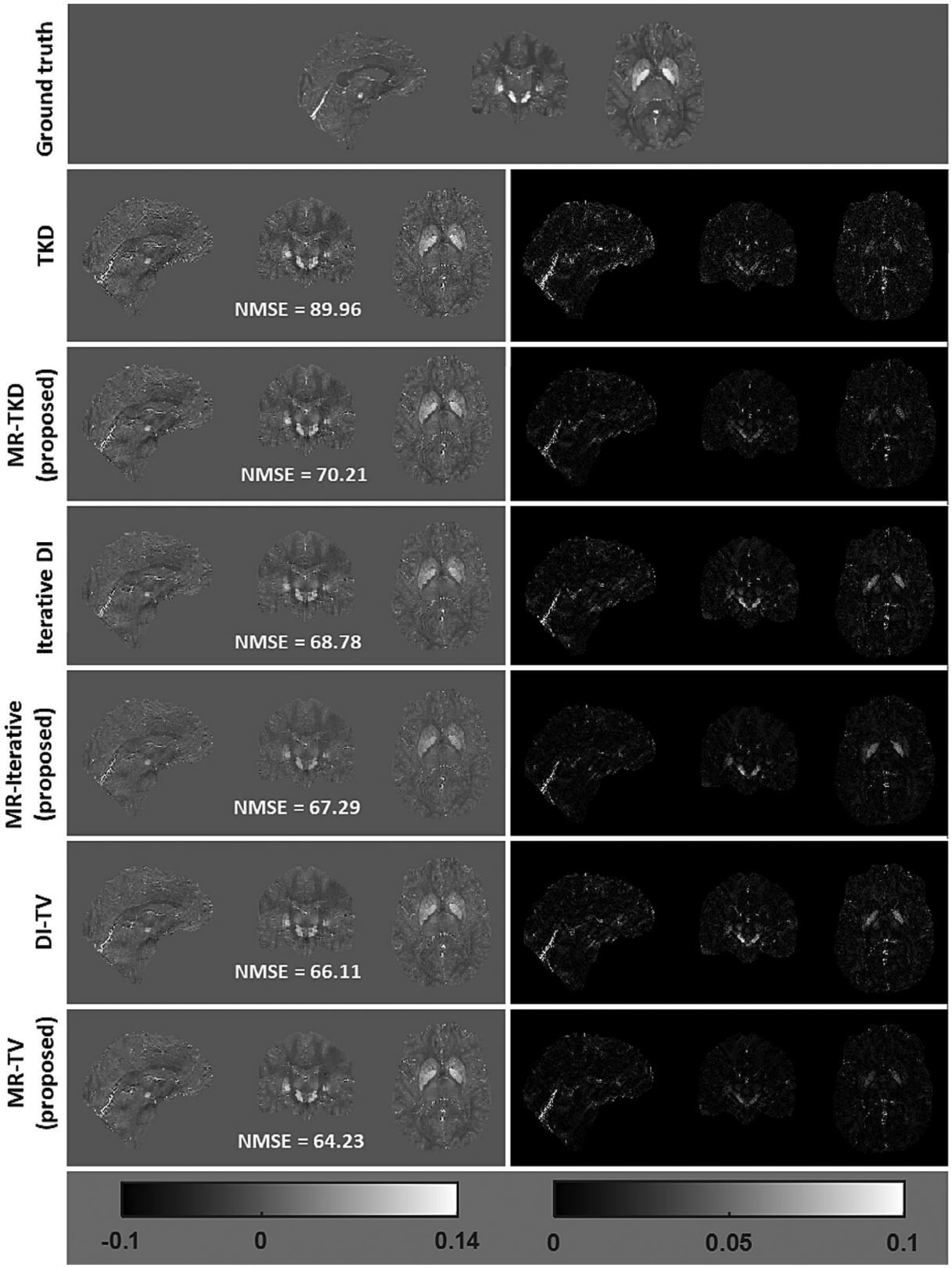

FIGURE 3 Reconstructed susceptibility maps (sagittal, coronal, and axial views) and corresponding difference images with respect to the ground truth susceptibility map obtained using the closed-form (rows 2 and 3), iterative (rows 4 and 5), and sparsity-enforced methods (rows 6 and 7) for reconstruction challenge2 (Sim1Snr1) data. The ground truth susceptibility maps are shown in the top row for reference. The respective NMSE values with respect to the ground truth susceptibility maps are also shown in the insets. DI, dipole inversion; DI-TV, dipole inversion with total variation prior; MR, iterative; MR-TKD, model resolution based truncated k-space division; MR-TV, model resolution deconvolution with total variation prior; NMSE, normalized mean squared error; TKD, thresholded k-space division.

TABLE 1 Average figure of merit and computed time over Dataset-I[13] (60 test volumes) and Dataset-II[17] (32 test volumes). The best figure of merit values are presented in bold.

	Dataset-I					Dataset-II				
Figure of merit	SSIM	PSNR (dB)	NMSE (%)	HFEN (%)	Time (s)	SSIM	PSNR (dB)	NMSE (%)	HFEN (%)	Time (s)
L2	0.8628	36.78	81.51	71.12	0.064	0.9122	32.46	83.29	67.39	0.058
MCF	0.8610	37.75	72.89	66.43	0.064	0.9132	32.85	69.16	62.80	0.075
SDI	0.8606	38.20	69.05	66.26	0.067	0.9153	32.85	66.11	63.57	0.068
TKD	0.8328	37.49	78.57	72.65	0.064	0.9098	32.05	70.21	67.14	0.072
MR-TKD (proposed)	**0.8714**	**38.47**	**67.90**	**64.19**	0.117	**0.9230**	**32.91**	**62.53**	**60.23**	0.139
Iterative DI	0.8747	38.46	66.58	64.45	1.70	0.9215	32.84	62.84	61.48	1.38
MR-iterative (proposed)	**0.8752**	**38.59**	**65.88**	**63.06**	1.69	**0.9233**	**32.93**	**62.06**	**59.64**	1.29
DI-TV	0.8778	38.48	65.74	63.35	3.74	0.9220	32.90	61.96	60.39	5.68
MR-TV (proposed)	**0.8802**	**38.93**	**64.03**	**61.96**	3.15	**0.9236**	**32.96**	**60.81**	**59.25**	5.05

Abbreviations: DI, dipole inversion; DI-TV, dipole inversion with total variation prior; HFEN, high-frequency error norm; MCF, modulated closed-form; MR, iterative; MR-TKD, model resolution based truncated k-space division; MR-TV, model resolution deconvolution with total variation prior; NMSE, normalized mean squared error; PSNR, peak signal-to-noise ratio; SDI, superfast dipole inversion; SSIM, structural similarity index measure; TKD, thresholded k-space division.

TABLE 2 Local measurements (mean value and standard deviation) of the susceptibility values (in parts per billion) across five head orientations for Subject-1 of Dataset-I.[13]

ROI	GP	PN	CN	SN	RN
L2	124.8 ± 39.5	62.4 ± 28.8	31.7 ± 29.3	48.10 ± 29.0	83.1 ± 17.6
TKD	110.4 ± 39.0	49.2 ± 25.4	35.0 ± 26.6	36.4 ± 31.2	78.5 ± 27.4
SDI	84.5 ± 27.2	38.1 ± 19.9	26.9 ± 17.8	32.3 ± 21.3	60.1 ± 18.1
MCF	113.1 ± 31.9	54.6 ± 24.6	30.4 ± 26.2	28.7 ± 27.3	81.8 ± 21.4
MR-TKD (proposed)	103.3 ± 32.7	46.1 ± 18.5	27.7 ± 23.4	35.3 ± 27.7	72.9 ± 23.2
Iterative DI	90.0 ± 23.2	42.4 ± 13.9	20.9 ± 16.7	39.3 ± 19.6	59.8 ± 17.0
MR-Iterative (proposed)	101.1 ± 31.1	45.5 ± 17.6	26.4 ± 21.5	40.8 ± 25.1	66.0 ± 21.7
DI-TV	91.8 ± 23.2	43.7 ± 14.6	25.3 ± 17.5	39.9 ± 19.5	61.0 ± 16.3
MR-TV (proposed)	104.1 ± 32.6	46.6 ± 18.6	24.4 ± 21.3	41.3 ± 24.6	69.2 ± 16.9
COSMOS	136.4	47.4	23.0	89.6	67.9

Abbreviations: CN, caudate nucleus; COSMOS, calculation of susceptibility through multiple orientation sampling; DI, dipole inversion; DI-TV, dipole inversion with total variation prior; GP, globus pallidus; MCF, modulated closed-form; MR, iterative; MR-TKD, model resolution based truncated k-space division; MR-TV, model resolution deconvolution with total variation prior; PN, putamen; RN, red nucleus; ROI, region of interest; SDI, superfast dipole inversion; SN, substantia nigra; TKD, thresholded k-space division.

in Figure S2 (B1) (Dataset-I) and (B3) (Dataset-II) also yielded an optimal τ value between 0.20 to 0.30 in all cases. It was also observed that the truncation parameter corresponding to the maximum CNR, as shown in Figure S2 (B2) and (B4), lies close to the optimal parameter. Because the optimal parameter has little variation across subjects, orientations, and acquisition protocols, we do not recommend repeatedly determining the parameter for each test case. In all our experiments, we utilized a truncation parameter of $\tau = 0.22$. The relative change in the figure of merit observed while choosing a heuristic truncation parameter $\tau = 0.22$ with respect to the optimal parameter is summarized in Table S2.

4.4 | Selection of scale factor and stopping criterion for iterative implementation

For the iterative implementation without regularization, plots of NMSE versus iterations are shown in Figure S3 for (A1) Subject-1 and (A2) Subject-2 (Dataset-I). Similarly, plots of NMSE versus iterations for Subject-1 and Subject-2 of Dataset-II are shown in Figure S3 (A3) and (A4), respectively. The minimum NMSE that can be achieved was found to be the same irrespective of the scale factor, in all cases. However, the rate of change is higher for larger values of the scale factor. In all experiments, a fixed scale factor of 0.10 was utilized. Plots of NMSE versus iterations for different subjects with the chosen scale factor are shown in Figure S3 (B1) (Dataset-I) and (B3) (Dataset-II). The corresponding

relative gradient norm versus iterations are shown in Figure S3 (B2) (Dataset-I) and (B4) (Dataset-II), respectively. The iterations were stopped when the relative gradient norm fell below 8.5, which was empirically chosen.

4.5 | Selection of scale factor and stopping criterion for sparsity-regularized implementation

For the sparsity-regularized implementation, plots of NMSE versus iterations are shown in Figure S4 for the (A1) Subject-1 and (A2) Subject-2 (Dataset-I). Similarly, plots of NMSE versus iterations for Subject-1 and Subject-2 of Dataset-II are shown in Figure S4 (A3) and (A4), respectively. Similar to the iterative implementation without regularization, the minimum NMSE that can be achieved was found to be the same irrespective of the scale factor, in all cases. However, the rate of change is higher for larger values of the scale factor. In all experiments, a fixed scale factor of 0.10 was utilized. Plots of NMSE versus iterations for different subjects with the chosen scale factor are shown in Figure S4 (B1) (Dataset-I) and (B3) (Dataset-II). It was observed that with regularization, the NMSE values exhibited a converging behavior as opposed to those without regularization. In all cases, the regularization parameter was empirically fixed as 10^{-4}. The corresponding relative gradient norm versus iterations are shown in Figure S4 (B2) (Dataset-I) and (B4) (Dataset-II), respectively. The iterations were stopped when the relative change in the successive iterates fell below 0.01 or the maximum number of iterations was reached, as indicated by the red circular markers in the NMSE plots.

4.6 | Application to other closed-form methods

The proposed model resolution-based deconvolution can be applied to other closed-form methods, like L2 and MCF. The figure of merit values obtained using these implementations are summarized in Table 3. It was observed that the proposed model-resolution deconvolution can improve the susceptibility map reconstructions compared with those of the original implementations.

5 | DISCUSSION

QSM has gained broad interest in the field because of its wide range of potential clinical applications.[30–32] However, the multiple processing steps involved in the QSM pipeline, which are fairly complex and computationally expensive, call for careful optimization, while employing the same in standard clinical practice. In this work, a two-step approach was proposed for improving the direct reconstruction approach in the context of TKD. This involves the computation of the TKD susceptibility map followed by a model resolution-based deconvolution to estimate a closer approximation to the true susceptibility map. Experiments demonstrated that the proposed approach compensates for the truncation of zero coefficients in the dipole kernel at the magic angle, thereby yielding more accurate reconstructions compared with other direct methods.

The proposed two-step formulation was utilized earlier in diffuse optical tomography[23] and photoacoustic tomography,[33] where the effect of regularization was lessened to provide better reconstructed images. In the QSM literature, a similar correction step to TKD was introduced in SDI[15] that utilizes the PSF due to dipole modification. The steps involved in TKD, MR-TKD, and SDI are summarized in Table S3 for easy reference. In SDI, the PSF was approximated as a delta function that enables rescaling of the TKD solution using $[PSF(\tau;\mathbf{0})]^{-1}$. Although $PSF(\tau;\mathbf{0})$ corresponds to its maximum value, there exist many nonzero values in the PSF. Consequently, there still remains some component of underestimation that further requires correction. Alternatively, all components of the model-resolution matrix have been utilized to perform the second deconvolution in the proposed model resolution-based deconvolution, which yields a closer approximation to the true susceptibility map than SDI.

TABLE 3 Average figure of merit over Dataset-I (60 test volumes) and Dataset-II (32 test volumes) without and with model-resolution deconvolution for L2-regularized and MCF reconstructions.

	Dataset-I				Dataset-II			
Figure of merit	**SSIM**	**PSNR (dB)**	**NMSE (%)**	**HFEN (%)**	**SSIM**	**PSNR (dB)**	**NMSE (%)**	**HFEN (%)**
L2	0.8628	36.78	81.51	71.12	0.9122	32.46	83.29	67.39
MR-L2	0.8660	37.18	76.05	65.66	0.9159	32.73	72.50	65.01
MCF	0.8610	37.75	72.89	66.43	0.9132	32.85	69.16	62.80
MR-MCF	0.8645	38.09	69.45	65.47	0.9153	32.95	65.56	62.10

Abbreviations: HFEN, high-frequency error norm; MCF, modulated closed-form; MR-L2, model resolution deconvolution after L2 reconstruction; MR-MCF, model resolution deconvolution after modulated closed form reconstruction; NMSE, normalized mean squared error; PSNR, peak signal-to-noise ratio; SSIM, structural similarity index measure.

6 | CONCLUSION

In this work, a two-step QSM reconstruction approach was established, wherein the model-resolution characteristics were utilized to reduce the artifacts introduced by the truncation of coefficients in the dipole kernel. The performance of the proposed model-resolution deconvolution for QSM reconstruction yields more accurate reconstructions compared with other direct and iterative methods across all datasets considered in the study.

ACKNOWLEDGMENTS

The authors are thankful to Dr. Jongho Lee, Laboratory for Imaging Science and Technology, Department of Electrical and Computer Engineering, Seoul National University, Seoul, South Korea, for providing the data. The authors are also thankful to Dr. Jeremias Sulam, Biomedical Engineering Department, Johns Hopkins University, for making their data[17] publicly available. The authors also acknowledge Dr. Carlos Milovic et al.[34] for making the FANSI code publicly available.

CONFLICT OF INTEREST STATEMENT

The authors declare no potential conflict of interest.

ORCID

Phaneendra K. Yalavarthy https://orcid.org/0000-0003-4810-352X

REFERENCES

1. Lee J, Shmueli K, Fukunaga M, et al. Sensitivity of MRI resonance frequency to the orientation of brain tissue microstructure. *Proc Natl Acad Sci*. 2010;107(11):5130-5135. doi:10.1073/pnas.0910222107
2. Wharton S, Bowtell R. Fiber orientation-dependent white matter contrast in gradient echo MRI. *Proc Natl Acad Sci*. 2012;109(45):18559-18564. doi:10.1073/pnas.1211075109
3. Langkammer C, Schweser F, Krebs N, et al. Quantitative susceptibility mapping (QSM) as a means to measure brain iron? *Neuroimage*. 2012;62(3):1593-1599. doi:10.1016/j.neuroimage.2012.05.049
4. Haacke EM, Liu S, Buch S, Zheng W, Wu D, Ye Y. Quantitative susceptibility mapping: current status and future directions. *Magn Reson Imaging*. 2015;33(1):1-25. doi:10.1016/j.mri.2014.09.004
5. Liu T, Spincemaille P, De Rochefort L, Kressler B, Wang Y. Calculation of susceptibility through multiple orientation sampling (COSMOS): a method for conditioning the inverse problem from measured magnetic field map to susceptibility source image in MRI. *Magn Reson Med*. 2009;61(1):196-204. doi:10.1002/mrm.21828
6. Liu C. Susceptibility tensor imaging. *Magn Reson Med*. 2010;63(6):1471-1477. doi:10.1002/mrm.22482
7. Shmueli K, de Zwart A, van Gelderen P, Li TQ, Dodd SJ, Duyn JH. Magnetic susceptibility mapping of brain tissue in vivo using MRI phase data. *Magn Reson Med*. 2009;62(6):1510-1522. doi:10.1002/mrm.22135
8. Bilgic B, Chatnuntawech I, Fan AP, et al. Fast image reconstruction with L2-regularization. *J Magn Reson Imaging*. 2014;40(1):181-191. doi:10.1002/jmri.24365
9. Liu T, Liu J, De Rochefort L, et al. Morphology enabled dipole inversion (MEDI) from a single-angle acquisition: comparison with COSMOS in human brain imaging. *Magn Reson Med*. 2011;66(3):777-783. doi:10.1002/mrm.22816
10. Liu J, Liu T, de Rochefort L, et al. Morphology enabled dipole inversion for quantitative susceptibility mapping using structural consistency between the magnitude image and the susceptibility map. *Neuroimage*. 2012;59(3):2560-2568. doi:10.1016/j.neuroimage.2011.08.082
11. Polak D, Chatnuntawech I, Yoon J, et al. Nonlinear dipole inversion (NDI) enables robust quantitative susceptibility mapping (QSM). *NMR Biomed*. 2020;33(12):e4271. doi:10.1002/nbm.4271
12. Rasmussen KGB, Kristensen M, Blendal RG, et al. DeepQSM-using deep learning to solve the dipole inversion for MRI susceptibility mapping. *BioRxiv*. 2018;278036.
13. Yoon J, Gong E, Chatnuntawech I, et al. Quantitative susceptibility mapping using deep neural network: QSMnet. *Neuroimage*. 2018;179:199-206. doi:10.1016/j.neuroimage.2018.06.030
14. Jung W, Yoon J, Ji S, et al. Exploring linearity of deep neural network trained QSM: QSMnet+. *Neuroimage*. 2020;211:116619. doi:10.1016/j.neuroimage.2020.116619
15. Schweser F, Deistung A, Sommer K, Reichenbach JR. Toward online reconstruction of quantitative susceptibility maps: superfast dipole inversion. *Magn Reson Med*. 2013;69(6):1581-1593. doi:10.1002/mrm.24405
16. Khabipova D, Wiaux Y, Gruetter R, Marques JP. A modulated closed form solution for quantitative susceptibility mapping—a thorough evaluation and comparison to iterative methods based on edge prior knowledge. *Neuroimage*. 2015;107:163-174. doi:10.1016/j.neuroimage.2014.11.038
17. Lai KW, Aggarwal M, Pv Z, Li X, Sulam J. Learned proximal networks for quantitative susceptibility mapping. *Med Image Comput Comput Assist Interv*. 2020;12262:125-135. doi:10.1007/978-3-030-59713-9_13
18. Li W, Wu B, Liu C. Quantitative susceptibility mapping of human brain reflects spatial variation in tissue composition. *Neuroimage*. 2011;55(4):1645-1656. doi:10.1016/j.neuroimage.2010.11.088
19. Smith SM. Fast robust automated brain extraction. *Hum Brain Mapp*. 2002;17(3):143-155. doi:10.1002/hbm.10062
20. Wu B, Li W, Guidon A, Liu C. Whole brain susceptibility mapping using compressed sensing. *Magn Reson Med*. 2012;67(1):137-147. doi:10.1002/mrm.23000

21. Özbay PS, Deistung A, Feng X, Nanz D, Reichenbach JR, Schweser F. A comprehensive numerical analysis of background phase correction with V-SHARP. *NMR Biomed*. 2017;30(4):e3550. doi:10.1002/nbm.3550
22. Zhdanov MS. *Geophysical inverse theory and regularization problems*. Vol. 36. Elsevier; 2002. doi:10.1016/S0076-6895(02)80037-3
23. Prakash J, Dehghani H, Pogue BW, Yalavarthy PK. Model-resolution-based basis pursuit deconvolution improves diffuse optical tomographic imaging. *IEEE Trans Med Imaging*. 2014;33(4):891-901. doi:10.1109/TMI.2013.2297691
24. Grabner G, Trattnig S, Barth M. Filtered deconvolution of a simulated and an in vivo phase model of the human brain. *J Magn Reson Imaging*. 2010; 32(2):289-297. doi:10.1002/jmri.22246
25. Wharton S, Schäfer A, Bowtell R. Susceptibility mapping in the human brain using threshold-based k-space division. *Magn Reson Med*. 2010;63(5): 1292-1304. doi:10.1002/mrm.22334
26. Wang Y, Liu T. Quantitative susceptibility mapping (QSM): decoding MRI data for a tissue magnetic biomarker. *Magn Reson Med*. 2015;73(1):82-101. doi:10.1002/mrm.25358
27. Steidl G, Weickert J, Brox T, Mrázek P, Welk M. On the equivalence of soft wavelet shrinkage, total variation diffusion, total variation regularization, and SIDEs. *SIAM J Numer Anal*. 2004;42(2):686-713. doi:10.1137/S0036142903422429
28. Langkammer C, Schweser F, Shmueli K, et al. Quantitative susceptibility mapping: report from the 2016 reconstruction challenge. *Magn Reson Med*. 2018;79(3):1661-1673. doi:10.1002/mrm.26830
29. QSM Challenge 2.0 Organization Committee, Bilgic B, Langkammer C, et al. QSM reconstruction challenge 2.0: design and report of results. *Magn Reson Med*. 2021;86(3):1241-1255. doi:10.1002/mrm.28754
30. Langkammer C, Liu T, Khalil M, et al. Quantitative susceptibility mapping in multiple sclerosis. *Radiology*. 2013;267(2):551-559. doi:10.1148/radiol.12120707
31. Langkammer C, Pirpamer L, Seiler S, et al. Quantitative susceptibility mapping in Parkinson's disease. *PLoS ONE*. 2016;11(9):e0162460. doi:10.1371/journal.pone.0162460
32. Fan AP, Evans KC, Stout JN, Rosen BR, Adalsteinsson E. Regional quantification of cerebral venous oxygenation from MRI susceptibility during hypercapnia. *Neuroimage*. 2015;104:146-155. doi:10.1016/j.neuroimage.2014.09.068
33. Prakash J, Raju AS, Shaw CB, Pramanik M, Yalavarthy PK. Basis pursuit deconvolution for improving model-based reconstructed images in photoacoustic tomography. *Biomed Opt Express*. 2014;5(5):1363-1377. doi:10.1364/BOE.5.001363
34. Milovic C, Bilgic B, Zhao B, Acosta-Cabronero J, Tejos C. Fast nonlinear susceptibility inversion with variational regularization. *Magn Reson Med*. 2018; 80(2):814-821. doi:10.1002/mrm.27073

SUPPORTING INFORMATION

Additional supporting information can be found online in the Supporting Information section at the end of this article.

How to cite this article: Mathew RS, Paluru N, Yalavarthy PK. Model resolution-based deconvolution for improved quantitative susceptibility mapping. *NMR in Biomedicine*. 2024;37(2):e5055. doi:10.1002/nbm.5055